ChemElectroChem

Research Article
doi.org/10.1002/celc.202201117

Chemistry Europe
European Chemical Societies Publishing

www.chemelectrochem.org



Special Collection

# Electrochemical Characterization of Charge Storage at Anodes for Sodium-Ion Batteries Based on Corncob Waste-Derived Hard Carbon and Binder

Luca Bottoni,*[a] Hamideh Darjazi,[a] Leonardo Sbrascini,[a] Antunes Staffolani,[a] Serena Gabrielli,[a] Genny Pastore,[a] Alessia Tombesi,[a] and Francesco Nobili[a, b]

Sodium-ion batteries (SIBs) represent a potential alternative to lithium-ion batteries in large-scale energy storage applications. To improve the sustainability of SIBs, the utilization of anode carbonaceous materials produced from biomass and the selection of a bio-based binder allowing an aqueous electrode processing are fundamental. Herein, corncobs are used as raw material for the preparation of hard carbon and it is also used as cellulose sources for the synthesis of carboxymethyl cellulose (CMC) binder. The corncob-derived electrodes deliver a high discharge capacity of around 264 $mAhg^{-1}$ at 1 C (300 $mAg^{-1}$), with promising capacity retention (84% after 100 cycles) and good rate capability. Additionally, this work expands the fundamental insight of the sodium storage behavior of Hard Carbons through an electrochemical approach, suggesting that the reaction mechanism is controlled by capacitive process in the sloping voltage region, while the diffusion-controlled intercalation is the predominant process in the low-voltage plateau.

## Introduction

Energy storage systems (ESSs) are drawing more and more attention for the worldwide utilization of intermittent renewable energy sources (such as wind, solar, wave, etc.), since they decrease the consumption of fossil fuels by enabling electric transportation.[1,2] Among ESSs, secondary batteries are ideal for numerous applications, and they represent promising devices.[3,4] Lithium-ion secondary batteries (LIBs) are widely used in portable electronic devices, power tools, and electrified vehicles[5] thanks to their high energy densities (up to 260 $Whkg^{-1}$ and 770 $WhI^{-1}$),[6] long cycle life, good rate capability and low self-discharge. However, there are concerns associated with the scale-up of MWh-class LIBs due to the limited abundance and odd distribution of lithium on Earth crust (are mainly located in remote and politically sensitive areas of South America).[2,7,8] Thus, the challenges related to lithium accessibility, together with the rapid growth of the electric vehicles market,[9] are expected to increase its price, giving uncertainty about the suitability of LIBs for other, less demanding applications, such as the stationary energy storage. In this context, sodium-ion batteries (SIBs) appear as a promising candidate for substitution of LIBs in stationary ESSs applications,[3] thanks to similar chemical properties of Na with Li, more than 1000 times higher abundance of Na resources than those of Li, wide distribution, and lower cost (0.50 $\$kg^{-1}$ for $Na_2CO_3$ vs 6.50 $\$kg^{-1}$ for $Li_2CO_3$).[2,10] Even if LIBs and SIBs share the same working principle,[11] there are some differences between these system. The larger ionic radius of $Na^+$ (1.02 Å) when compared to $Li^+$ (0.76 Å) affects the transport properties and phase stability,[4] while the higher standard potential of −2.71 V for $Na^+$/Na and the heavier molecular weight of Na in contrast with Li (with a redox potential of −3.01 V and a molecular weight of 6.9 $gmol^{-1}$), prevent high theoretical specific capacity and energy density.[12] Nevertheless, the mass of the charge carrier represent a small fraction of the overall mass of the cell components, thus the gap in energy density can be in practice mitigated by selecting high capacities host structures along with high operating potential interval between cathode and anode (i.e. high cell output voltage).[13] Considering that the energy density of C/$LiFePO_4$ 18650 size commercial LIBs is around 130 $Whkg^{-1}$, a same size and fully developed Na-ion battery can reach 150 $Whkg^{-1}$ at best, making it suitable for replacing $LiFePO_4$ batteries.[14] Significant successes have been achieved in the development of cathode materials for SIBs, which mainly include layered transition-metal oxides, polyanionic compounds and metal hexacyanometalates. However, the identification of suitable anode materials still remains challenging for the development of SIBs[1,4] because of the poor Na storage capability by graphite. This is due to larger ionic size of sodium and thermodynamic instability of sodium–graphite intercalation compounds, resulting in poor electrochemical performances.[15] To the best of our knowledge, the best results

[a] L. Bottoni, Dr. H. Darjazi, L. Sbrascini, Dr. A. Staffolani, Prof. S. Gabrielli, Dr. G. Pastore, Dr. A. Tombesi, Prof. F. Nobili
School of Science and Technology, Chemistry Division
University of Camerino
Via Madonna delle Carceri-ChIP, Camerino (MC) 62032 (Italy)
E-mail: luca.bottoni@unicam.it
[b] Prof. F. Nobili
GISEL – Centro di Riferimento Nazionale per i Sistemi di Accumulo Elettrochimico di Energia
INSTM
Via Giuseppe Giusti 9, Firenze (FI) 50121 (Italy)

Special Collection An invited contribution to a Special Collection dedicated to Giornate dell'Elettrochimica Italiana 2022 (GEI2022)

obtained up to now with graphite anodes in SIBS are limited to 150 $mAhg^{-1}$[16] when using ether-based electrolytes. However, this performance is far from that obtained with LIBs analogues.[17]

Therefore, different types of anode materials have been proposed: alternative carbonaceous materials, metal oxides, alloys and organic compounds.[18] Among them, Hard Carbons (HCs) are the state of the art anode material for SIBs[4,19] thanks to their promising overall performance, relatively low cost, wide availability, and low operating voltage of ~0.1 V *vs.* $Na^+/Na$.[20] HCs, also known as disordered or amorphous carbons, are composed by arrangements of graphene sheets stacked in the short-range due to the Van Der Waals forces, but randomly oriented in the long-range.[19] HCs are generally produced by thermal decomposition of synthetic organic compounds and biomass precursors. Lately, lignocellulosic materials (i.e., agricultural and forestry by-products) are considered the best choice as hard carbon precursors thanks to their environmentally-benign and cost-effective features.[19] Several lignocellulosic precursors have been used for synthesize HCs for SIBs such as wood,[21] lignin,[22] peanut and hazelnut shells,[23,24] pinecone,[25] sugarcane bagasse,[26] pomelo and banana peels,[27,28] olive leaves[29] and lotus stem.[30] Among them, corncob, the core of an ear of maize, represent an abundant and readily available lignocellulosic waste considering that the maize has the largest production globally with an estimate production of 1026 million tons per year and the corncob account for around the 22% of its weight. Since corncobs are low-value by-products, their management usually involves the landfilling and open-air burning, producing greenhouse gases and air pollution.[31] Therefore, using corncobs as raw material to improve the sustainability of SIBs is particularly appealing.

Typically, the sodium storage mechanism in HCs involves two distinct voltage regions: a sloping potential region (up to 0.1 V *vs.* $Na^+/Na$) and a low potential plateau (< 0.1 V *vs.* $Na^+/Na$);[32] however, the assignment of these regions to a specific sodium storage mechanism is still controversial, considering the complexity of hard carbon structure which implies the presence of heteroatoms, defects, edges, lateral size and thickness of graphitic domains and micropores in their structures.[33] In 2000, Steven et al. proposed the model of "intercalation-adsorption" for HCs upon sodiation/desodiation process, meaning the insertion of $Na^+$ ions between the layers at high potential, and adsorption of ions in micropores at low potential.[34] By contrast, recent experimental findings have suggested the model of "adsorption-intercalation", meaning the adsorption of $Na^+$ ions occur in the high-potential, while low-potential plateau corresponds to intercalation between layers.[33] More recently, the so-called "three-stage model" was proposed by Bommier et al. which involves the adsorption at surfaces sites in the sloping region followed by the intercalation between graphene layers in the low-voltage plateau and pore filling at the end of the plateau region.[35,36] Finally, Zhang et al. present the "adsorption-filling model", where the sodium storage is governed by the adsorption of $Na^+$ at defect sites and disordered isolated graphene sheets in the sloping region, while the plateau capacity is due to the mesopore filling.[37,38] Thus, in order to improve the understanding of the redox mechanisms and the performances of HC materials, more extensive studies are required, due to the inconsistency of the reported works.

Besides, the selection and optimization of the binder is crucial to develop SIBs,[39] since it ensures the adhesion between the electrode materials and the current collector and binding the active material grains with the conductive agent, guaranteeing the electrode stability and cycle life.[40] Moreover, keeping the focus on batteries sustainability, the use of bio-based and aqueous electrode processing is particularly appealing since they can bring down the costs and environmental impacts of electrode manufacture. Among the aqueous binders, the sodium salt of carboxymethylcellulose (Na–CMC) is a cheap cellulose derivative which represents an important alternative to the expensive, toxic, and non-aqueous polyvinylidene fluoride (PVDF), the *de-facto* standard binder of LIBs.[39,41] Na–CMC is obtained reacting the cellulose with chloroacetic acid or its sodium salt in NaOH environment. Na–CMC properties depend strongly on the degree of substitution (DS): generally lower DS results in higher hydrophobicity and thus stronger interactions with carbon materials.[39]

In this context, corncobs were used as raw materials both for the preparation of HC with a simple one-step thermal treatment and as cellulose source, which was then converted to sodium carboxymethylcellulose (Na–CMC). Apart for an additional way to reuse lignocellulosic waste, the in-house synthesis of CMC binder can be advantageous since the DS can tuned accordingly to the active material used, enhancing the electrode stability. Then, the two materials were combined and used for the fabrication of composite SIB anodes. The electrochemical performances of the corncob-waste derived electrode and the mechanisms of sodium storage into HC were investigated in Na half-cells.

## Results and Discussion

### Synthesis, Chemical and structural characterization of the corncob-derived carboxymtehylcellulose (CC–CMC) binder

Carboxymethyl cellulose has been synthesized from corncob food waste as raw material by the procedure detailed in the Experimental Section. The NaOH alkaline pretreatment and subsequent NaClO bleaching were used to dissolve lignin and hemicellulose,[42] while HCl treatment was aimed to isolate the crystalline part of cellulose.[43] Then, the extracted cellulose was submitted to alkalinization with NaOH and etherification with monochloroacetic acid. According to the scheme proposed by Shui et al. in alkalization, the cellulose is converted to sodium cellulosate, as shown in Eq. (1), while in etherification, monocholoroacetic acid is firstly converted to sodium monochloroacetate Eq. (2) and then undergoes to nucleophilic substitution at chlorine site, forming Na–CMC Eq. (3):[44]

$$[C_6H_7O_2(OH)_3]_n + nNaOH \rightarrow [C_6H_7O_2(OH)_2ONa]_n + nH_2O \quad (1)$$

$$ClCH_2COOH + NaOH \rightarrow ClCH_2COONa + H_2O \quad (2)$$

$$[C_6H_7O_2(OH)_2ONa]_n + nClCH_2COONa \rightarrow n[C_6H_7O_2(OH)_2OCH_2COONa] + nNaCl \quad (3)$$

The final product has been labelled as CC–CMC. The reference commercial product is hereafter labelled as ST–CMC.

FT-IR spectra of the extracted cellulose, CC–CMC and ST–CMC are reported in Figure 1a. The wide peaks around 3340 $cm^{-1}$ and 2890 $cm^{-1}$ in all samples can be assigned to the stretching vibration of O–H groups in glycosidic units and the C–H group stretching, respectively, indicate the cellulose backbone. The presence of a strong absorption band at ~1597 $cm^{-1}$ in the CC–CMC sample corresponds to the carboxyl stretching $COO^-$, conforming the carboxymethylation.[45,46] The peaks at about 1422 and 1319 $cm^{-1}$, present in both CMC samples, are related to the $–CH_2–$ scissoring and –OH bending vibration, respectively.[47] The peak at ~1040 $cm^{-1}$ is attributed to the C–O stretching of ether and alcohol in glucose units in all samples.[44]

In order to investigate the thermal stabilities of synthesized CC–CMC and commercial ST–CMC, TGA was carried out (Figure 1b). The thermal degradation pattern of CC–CMC has a similar trend than the reference compound. In both samples, the first degradation step around 100 °C is associated with the evaporation of water. The main weight loss (~41%) for CC–CMC starts at an onset temperature of 230 °C and continues until 305 °C. This step can be mainly related to the decarboxylation of cellulose[48] followed by the onset of breaking down of cellulose chains into lower molecular weight hydrocarbons. The cellulose backbone decomposition is the main process evidenced in the range 305–600 °C,[49] with a weight loss of around 25%. Above 600 °C, the residual liquid and solid char evolve into a gaseous fraction leaving around 10% of ash content.

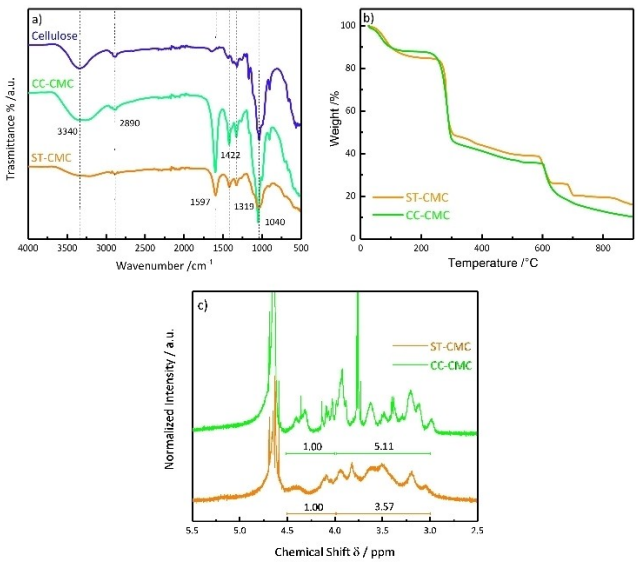


**Figure 1.** Chemical Characterization of CMC. (a) FT-IR spectra of Cellulose, CC–CMC, and ST–CMC; (b) TGA data of CC–CMC, and ST–CMC; (c) NMR spectra of CC–CMC and ST–CMC.

Since the physical-chemical properties of CMC are affected by the degree of substitution (DS), the DS was estimated using $^1$H-NMR spectroscopy. Figure 1c illustrates $^1$H-NMR spectrum of CC–CMC in $D_2O$. The CMCs spectral lines in the range 4.5–3.0 ppm are very complicated, making the assignment of $^1$H chemical shifts and the extrapolation of structural information very difficult. The DS value of the CC–CMC samples has been estimated as 0.59, in agreement with Shui et al.[44] which used the same NaOH/$ClCH_2COOH$ molar ratio for the etherification. The DS value of ST–CMC has been estimated as 0.84 (vs. 0.9 declared by the manufacturer), thus assessing a quite good reliability of the analytical method.

## Chemical, structural and morphological characterization of the corncob-derived hard carbon (CCDHC) active material

The SEM image in Figure 2 shows that the CCDHC is characterized by blocklike morphology with irregular particles size in the micrometer range.[50] The elemental composition estimated by EDX analysis reveals that, apart from carbon (95.9 at%) and oxygen (1.6 at%), there are residual potassium impurities (2.5 at %), which is originated from the biomass matrix.

The structure of CCDHC was evaluated by XRD, as shown in Figure 3a. Two broad peaks can be observed at 2θ values of 23° and 43°, which correspond to the crystallographic planes of (002) and (100) in the disordered carbon structure, respectively. No impurity peaks were observed from XRD pattern. Crystallographic parameters acquired by XRD analysis are presented in Table 1. According to the Bragg's Law, the $d_{002}$ interplanar

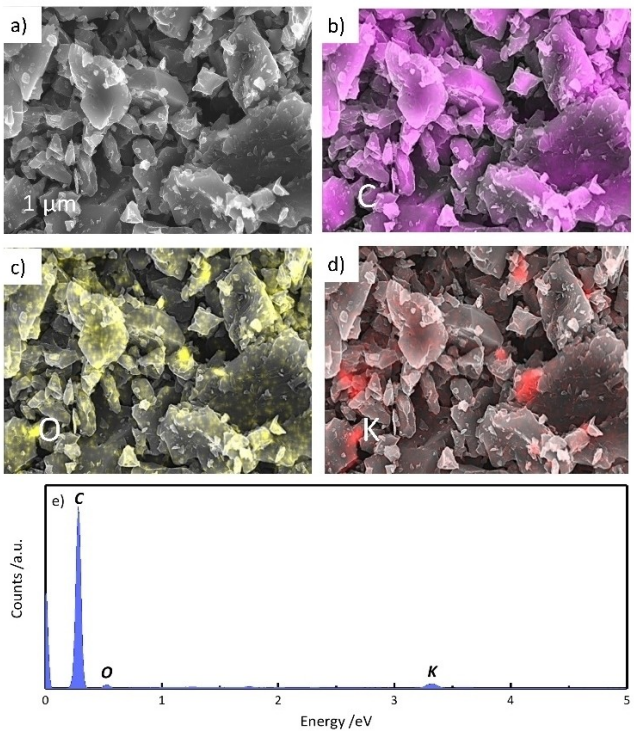


**Figure 2.** (a) SEM image of CCDHC; EDX elemental mapping of (b) carbon; (c) oxygen; (d) potassium; Magnification = 5000x. (e) EDX analysis of CCDHC.

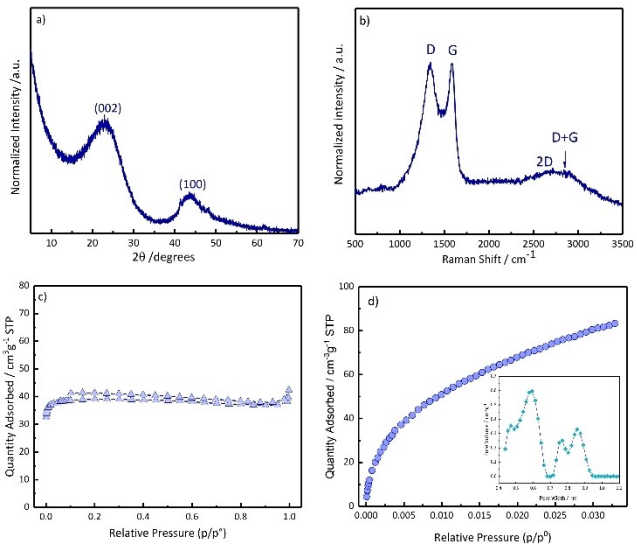


**Figure 3.** Chemical and physical characterization of CCDHC powder: (a) XRD pattern; (b) Raman spectra; (c) $N_2$ adsorption-desorption isotherm; (d) $CO_2$ adsorption isotherm and pore size distribution.

**Table 1.** Crystallographic parameters of CCDHC powder.

| Sample | $d_{002}$ | $L_c$ [nm] | $L_a$ [nm] | $I_G/I_D$ | *n* |
|---|---|---|---|---|---|
| CCDHC | 0.387 | 0.78 | 19.14 | 0.996 | 3.01 |

spacing is calculated as 0.387 nm, which is higher than that of graphite (0.335 nm), facilitating the sodium insertion/de-insertion between graphene layers.[51] The staked plane height ($L_c$) can be approximately estimated as 0.78 nm from XRD peaks, respectively, which are close to those of the reported $sp^2$ carbon.[30,52] The number of interlayers stacked in the graphitic domains *n* can be roughly estimated using $d_{002}$ (0.387 nm) and $L_c$ (0.780 nm) values. According to the calculation ($n = 0.780/0.387 + 1$) the graphitic domain of CCDHC is made up of 3 stacked graphene layers.[53] To further investigate the carbon textural characteristics, the Raman spectrum of CCDHC powder was performed. As shown in Figure 3b, the powder shows two peaks at around 1344 $cm^{-1}$ (D-band) and 1587 $cm^{-1}$ (G-band), which are characteristic for all layered carbon materials. The D-band originates from disordered and defective $sp^3$ carbons while the G-band corresponds to graphitic in-plane $sp^2$ carbons.[54] The intensity ratio between the G band over the D band ($I_G/I_D$) reflects the disordered degree of hard carbon materials, which is calculated to be 0.996, indicating the low degree of graphitic ordering of CCDHC powder (Table 1).[23] Moreover, two broad and small peaks are located at ~2690 $cm^{-1}$ and 2900 $cm^{-1}$, which correspond to 2D and D + G bands, respectively. The 2D band is associated with the degree of graphitization and the D + G band is associated with defect activated process for an elastic scattering.[55,56] An $L_a$ value of 19.14 nm is calculated from Raman band analysis, according to Eq. (4). To fully understand the pore structures of CCDHC, two different probing molecules ($N_2$ and $CO_2$) were used. Firstly, $N_2$ adsorption-desorption measurement was conducted and the obtained isotherm is showed in Figure 3c. According to the International Union of Pure and Applied Chemistry (IUPAC) classification, this graph is the consistent with a type IV isotherm typical of mesoporous materials with a hysteresis loop at a relative pressure in the range 0.15–1 $p/p^0$. Moreover, the sharp rise at low relative pressure ($< 0.14\ p/p^0$) denotes the presence of micropores.[57,58] The Brunauer-Emmett-Teller (BET) surface area was determined to be 124.4 $m^2 g^{-1}$. Considering that $N_2$ is not suitable for the determination of small size pores (< 0.7 nm), the ultramicroporosity determination was achieved using $CO_2$ at higher temperature (273 K) favoring the gas diffusion into the narrowest pores.[59] The $CO_2$ adsorption isotherm is showed in Figure 3d. The results showed that the $CO_2$ BET surface area is significantly higher respect to $N_2$ BET (427.2 $m^2 g^{-1}$ vs 124.4 $m^2 g^{-1}$) suggesting an extra-porosity coming from the ultramicropores. The same behavior was observed on other types of hard carbons.[55,59] The DFT pore size distributions confirm the presence of micropores with peaks at 0.47, 0.60, 0.77 and 0.85 nm and a total volume of micropores of 0.11 $cm^3 g^{-1}$.

## Electrochemical Characterization

The galvanostatic charge/discharge E vs. Q profiles of the CCDHC/CC–CMC composite electrodes, cycled at a current density of 300 $mAg^{-1}$ between 0.01 and 2 V in half cell, are displayed in Figure 4a, and reveal the typical features of Na storage by amorphous carbon, i.e. a potential sloping region extending down to 0.1 V followed by a low potential plateau below 0.1 V. During the first discharge process, a pseudo plateau starting at 0.9 V evidences electrolyte decomposition and solid electrolyte interphase (SEI) formation, which lead to an irreversible capacity loss of 165.43 $mAhg^{-1}$. This pseudo plateau disappears in the subsequent cycles suggesting that a relatively stable SEI is formed.[60] The CCDHC electrode shows a reversible specific capacity above 200 $mAhg^{-1}$ for more than 400 cycles, confirming the high reversibility of the sodiation processes. To investigate the contribution of the sloping region and of the low-voltage plateau to the overall Na storage, dQ/dV curves at different cycles were plotted (Figure 4b). As shown, $E_{we} = 0.1$ V can be considered as the discrimination point during sodiation between sloping (above 0.1 V) and plateau (below 0.1 V) regions. Thus, the discharge capacities of selected cycles were separated in these two regions, as shown in Figure 4c. It is interesting to note that the contribution of the low-voltage plateau to the capacity remains practically constant through cycling (around 120 $mAhg^{-1}$), representing a high reversibility of the Na storage processes occurring at the low-voltage plateau. On the other side, the contribution of the sloping region progressively decreases upon cycling (it passes from 136.7 $mAhg^{-1}$ of the 2nd cycle to 85.9 $mAhg^{-1}$ of the 400th cycle), suggesting a partial irreversibility of the step. The charge/discharge capability and capacity retention of three different cells cycled at 1 C, 2 C, 5 C, respectively, are shown in Figure 4d, as well as the corresponding Coulombic efficiencies. The electrodes cycled at 1 C, 2 C, and 5 C evidence initial discharge

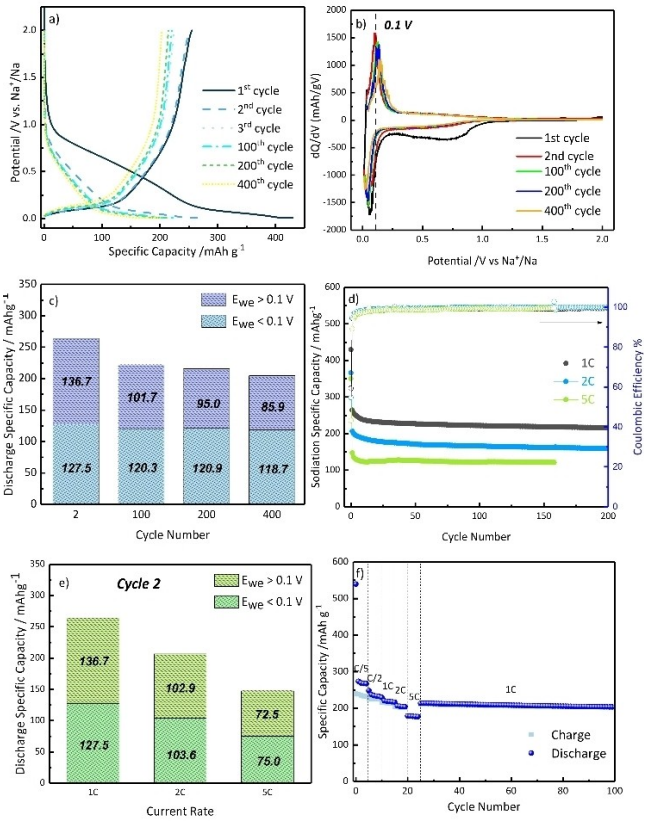


**Figure 4.** Electrochemical performances of CCDHC-based SIB electrode prepared with CC–CMC binder: (a) Galvanostatic discharge/charge voltage profile at 1 C; (b) dQ/dV vs $E_{we}$ curves at different cycles; (c) Contribution to capacity above and below 0.1 V as a function of cycle number; (d) Long cycling at different scan rates (1 C, 2 C and 5 C); (e) Contribution to capacity above and below 0.1 V as a function of current density at 2nd cycle; (f) Rate capability.

capacity of 429.7, 366.0, and 350.2 $mAhg^{-1}$, with corresponding initial Coulombic efficiencies (ICE) of 59.4%, 54.7%, and 43.2%, respectively (see Table 2). Caution has to be exercised in interpreting this apparently strange ICE trend, since the complete formation of the SEI requires more than one cycle, making the definition of a trend quite difficult. Nonetheless, the CCDHC exhibit ICE in line with most hard carbon materials, which have ICE in the range 40–70%.[61] However, in full-cell configuration the irreversible loss of cyclable sodium must be compensated by the cathode material, reducing the energy density of cell and limiting the practical applications of SIBs. Therefore, improving the ICE is a key issue for the development of commercial sodium-ion batteries.[62] During the second cycle, the electrodes exhibit discharge capacities of 264.3, 206.6, and 147.5 $mAhg^{-1}$ with an excellent capacity retention of 84.0%, 80.4%, and 82.9% after 100 cycles at 1 C, 2 C, and 5 C, respectively. Figure 4e shows the contribution of capacity above and below 0.1 V at different current rates. The low-voltage contribution increases slightly slower (so that the percentage contributions increase from 48.26% at 1 C to 50.16% at 2 C and 50.85% at 5 C), suggesting that, due to the increasing of cell polarization at higher current rates, there is a possible contribution of the fast surface-controlled capacitive process of sodium storage also in the low-voltage plateau. To further evaluate the charge/discharge capability of the electrode at various currents, a fresh cell was subjected to rate capability measurements in the cycling rate from C/5 to 5 C, as shown in Figure 4f. The CCDHC electrode exhibits a promising rate capability with a low-capacity fade when the current is boosted, ranging from 273.9 $mAhg^{-1}$ at C/5 to 179.2 $mAhg^{-1}$ at 5 C. Afterwards, the capability to recover pristine performances was investigated by cycling the electrode at 1 C up to 100 overall cycles. The cell yields a specific capacity above 200 $mAhg^{-1}$ after 100 cycles, suggesting outstanding reversibility and stability even in demanding conditions. Comparing these results with others found in literature, CCDHC shown superior or comparable performances in terms of specific capacity and rate capability respect to other biomass-derived HCs.[18,26,50,52,63,64] Moreover, the synthesis of the CMC binder from the same abundant raw material, which has a high cellulose content (around 69%),[31] can additionally improve the sustainability of the electrode manufacture especially through aqueous electrode processing. However, it is worth to note that testing materials in half-cell configuration may be not truly representative and can eventually underrate the performances of active materials due to the high reactivity of sodium metal counter and reference electrodes in organic electrolytes, which can influence the electrode/electrolyte interface stability and resistance and thus the cycle life.[65,66]

In order to investigate the nature of Na storage processes in the CCDHC electrode, cyclic voltammetry (CV) experiments were performed. Firstly, CV of the initial three cycles was run at a scan rate of 0.1 $mVs^{-1}$ between 0.01 and 2 V in a half cell *vs.* $Na^+/Na$, as shown in Figure 5a. The irreversible broad peak at the first cathodic scan centered at 0.57 V (A) can be assigned mostly to the decomposition of the electrolyte and the formation of the SEI.[67] In the following scans, the contribution from irreversible SEI formation disappears, leaving a broad feature (B) due to the "high-potential" ($E > 0.1$ V) Na storage. This is a reversible process, as confirmed by the symmetrical B' feature revealed during anode scans. The sharp reversible peak near 0.01 V is attributed to the $Na^+$ insertion/extraction into hard carbon.[30] After the 1st cycle, the CV curves are overlapped, indicating a reversible electrochemical behavior. To provide a deeper understanding of the Na storage surface-related capacitive and bulk-related diffusive behaviors, cyclic voltammetries were also recorded at different scan rates between 0.1 $mVs^{-1}$ and 1.0 $mVs^{-1}$ (Figure 5b). All the CV curves show similar shapes at various sweep rates, and a small polarization of the anodic and cathodic peaks can be seen evidenced during

**Table 2.** First-cycle irreversible capacity, initial coulombic efficiency (ICE), second-cycle reversible discharge capacity, and capacity retention of CCDHC-based SIB electrodes at different current rates.

| Current Rate | Discharge Capacity 1st cycle [$mAhg^{-1}$] | ICE [%] | Discharge Capacity 2nd cycle [$mAhg^{-1}$] | Capacity Retention after 100 cycles [%] |
|---|---|---|---|---|
| 1 C | 429.7 | 59.4 | 264.3 | 84.0 |
| 2 C | 366.0 | 54.7 | 206.6 | 80.4 |
| 5 C | 350.2 | 43.2 | 147.5 | 82.9 |

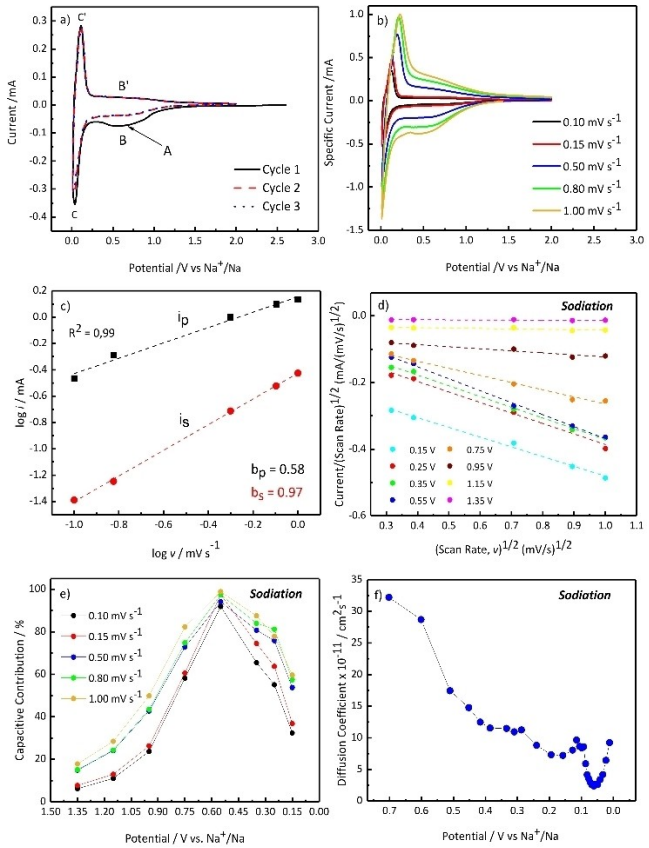


**Figure 5.** Electrochemical performances of CCDHC-based SIB electrode prepared with CC–CMC binder: (a) Cyclic Voltammetry upon the first three cycles, scan rate 0.1 mV $s^{-1}$; (b) CV curves at different sweep rates (between 0.1 mV $s^{-1}$ and 1 mV $s^{-1}$); (c) Relationship between log *i* and log *v*; (d) $i(V)/v^{1/2}$ against $v^{1/2}$ at different potentials during sodiation; (e) capacitive contribution % during sodiation as a function of the potential at different scan rates; (f) Diffusion coefficient at different potentials during sodiation.

the charge and discharge.[68] In order to determine the sodium storage mechanism, the power-law relationship between scanning rate and peak currents was calculated by fitting the experimental data to the following equations Eq. (4) and Eq. (5):[69]

$$i = av^b \tag{4}$$

$$\log i = b\log v + \log a \tag{5}$$

Where *i* and *v* show the peak current and the scanning rate, respectively, while *a* and *b* are the parameters to be determined. Typically, a value of *b* close to 0.5 indicates a diffusion-controlled reaction, such as insertion/extraction between graphene layers, while a value of *b* close to 1 indicates that the current is controlled by a capacitive behavior.[69] Two peaks were selected for the kinetic analysis: the first one is the broad peak at 0.5 V ($i_j$) corresponding to the sloping region, while the second one is the sharp peak in the low potential region at 0.01 V ($i_p$). The current peaks as a function of the scan rate in logarithmic scale are shown in Figure 5c, representing an excellent linear relationship with $R^2 = 0.99$ for both curves, with a slope of 0.97 for $i_j$ and 0.58 for $i_p$, respectively. Thus, these results suggests that the current in the sloping region ($i_j$) arises from the surface controlled reactions (i.e. adsorption on active sites) while the current at low-potentials ($i_p$) originates from the diffusion-controlled reaction (i.e. sodium insertion/extraction between graphene layers).[70–73] Additionally, the capacitive contribution to the current response can be determined according to the following equation Eq. (6):

$$i(V) = k_1 v + k_2 v^{1/2} \tag{6}$$

where the current response at a fixed potential can be distinguished in surface-controlled ($k_1 v$) and diffusion-dependent ($k_2 v^{1/2}$) contributions. By counting $k_1$ and $k_2$, the split of the contribution of the two mechanisms to the current response can be determined.[72,74] Figure 5d shows the excellent linear relationship of $i(V)/v^{1/2}$ against $v^{1/2}$ at different potentials during the sodiation process, which were used for the determination of $k_1$ (slope) and $k_2$ (intercept)., Figure 5e shows the trends of capacitive contribution (%) at different scan rates (*v*) as a function of potential (V), as calculated from Eq. (6). As expected, increasing the sweeping rate leads to a higher pseudocapacitive contribution at each potential step, meaning that the current response comes from the fast surface-induced capacitive process, such as adsorption.[58,75] It is interesting to note that starting from 0.15 V, the capacitive contribution increases reaching a maximum at 0.55 V (91.9% at 0.1 $mVs^{-1}$ and 98.9% at 1.0 $mVs^{-1}$) and then decreases rapidly reaching a minimum at 1.35 V (6.2% at 0.1 $mVs^{-1}$ and 17.8% at 1.0 $mVs^{-1}$) at each scan rate. These results confirm that at $E_{we} \leq 0.15$ V the uppermost process is the diffusion-controlled intercalation of sodium into carbon framework, however there is a small contribution of capacitive process especially at high current density; at $0.25 \leq E_{we} \leq 0.75$ V the surface-controlled processes are predominant.

The kinetics of $Na^+$ diffusion in CCDHC was investigated by Galvanostatic Intermittent Titration Technique (GITT), applying a current pulse of 30 $mAg^{-1}$ for 0.5 h followed by 3 h of relaxation for each current pulse. According to the Fick's second law, the diffusion coefficient $D_{Na+}$ values were calculated using the following equation Eq. (7):

$$D_{Na^+} = \frac{4}{\pi\tau}\left(\frac{m_b \cdot V_m}{M_b \cdot S}\right)^2 \left(\frac{\Delta E_s}{\Delta E\tau}\right)^2 \tag{7}$$

Where $\tau$ is the current pulse time (s), $m_b$ is the mass of the active material (g), $V_m$ and $M_b$ represent the molar volume ($cm^3mol^{-1}$) and molar mass ($gmol^{-1}$) of carbon, respectively, S is the contact surface area of the electrode ($cm^2$), $\triangle E_s$ is the steady-state voltage change during a single step of GITT and $\triangle E_\tau$ is the voltage change during a single current pulse.[52] The calculated diffusion coefficient during sodiation ($D_{Na}{}^+$) was plotted as a function of voltage, as shown in Figure 5f. The high values of $D_{Na}{}^+$ of CCDHC in the high part of the sloping region ($E_{we} > 0.3$ V) mimic the rapid adsorption of sodium ions on surface active sites, which are gradually occupied during sodiation leading to a progressive decrease of $D_{Na}{}^+$. In the lower part of the sloping region ($0.3 < E_{we} < 0.1$ V), the saturation of

the surface accessible sites forces the remaining sodium ions to increase the diffusion length to find vacant adsorption sites, decreasing the diffusion coefficient to values in the order of $10^{-11}$ $cm^2 s^{-1}$.[58] Finally, in the low-voltage plateau ($E_{we} < 0.1$ V), the apparent diffusion coefficient rapidly decreases reaching a minimum at $E_{we} = 0.06$ V because the sodium ions have to overcome the energy barrier to intercalate between graphene layers. After that, since the interlayer spacing is enhanced by the intercalated sodium ions, the diffusion coefficient rapidly recovers before the cutoff potential, indicating an easier diffusion kinetic.[76]

A deeper study of the kinetics of the charge/discharge processes as well as the interfacial behavior of the electrode have been performed through electrochemical impedance spectroscopy (EIS) measurements every 10th cycle at $E_{we} = 0.5$ V. The Nyquist plots are shown in Figure 6a. All the impedance spectra present similar features: (i) a semicircle in the high-frequency region related to sodium migration through SEI film, which is partially overlapped by (ii) a semicircle in the middle-frequency region correlated with the interfacial charge-transfer process;[77] (iii) a straight line in the low-frequency region corresponding to the $Na^+$ ion diffusion in the bulk of electrode material.[68] EIS data were fitted through an equivalent circuit model, noted as $R_{el}(R_{SEI}C_{SEI})(R_{ct}C_{dl})WC_i$ in the notation of Boukamp.[56] The calculated values of $R_{SEI}$ and $R_{ct}$ are shown in Figure 6b. The $R_{el}$, $R_{SEI}$ and $R_{ct}$ are the resistances associated with electrolyte, SEI passivation layer and charge-transfer process, while $C_{SEI}$, $C_{ct}$ and $C_i$ are the SEI film capacity, electric double layer capacity and differential intercalation capacity, respectively. W is the Warburg element, describing $Na^+$ diffusion.[56] For the fitting procedure, the pure capacitive elements were replaced by constant phase elements Q to take into account the non-ideal capacitive behavior given by the electrode surface roughness and inhomogeneity.[78] The electrode exhibits low resistance ($R_{SEI}$ and $R_{ct}$) values upon cycling, indicating high reaction kinetics and interfacial stability. As regards the passivation layer, the calculated $R_{SEI}$ values slightly increase during the first 30 cycles, and then remains almost unchanged during the subsequent ones, suggesting strong interactions of the CC–CMC binder with carbon substrate[39,79] and SEI products. However, the dynamic nature of the SEI formation leads to continuous partial dissolution and re-formation of the outer layer of the SEI, which is soluble in carbonate electrolytes.[80,81] Therefore, the formation of a stable passivation layer requires some cycles. As regards the charge-transfer resistance, during the first cycles the electrode shows higher $R_{ct}$ values with respect to subsequent cycles, probably because of an electrode activation due to progressive pore surface wetting by the electrolyte. The calculated $R_{ct}$ values decrease after 20 cycles and remain unchanged up to 100 cycles, evidencing the stabilization of the electrode/electrolyte interface.

To further evaluate the redox processes occurring at Hard Carbon, distribution of relaxation times analysis (DRT) was applied to the impedance spectra collected during sodiation and desodiation (5th cycle). The raw spectra evidenced the same features observed in Figure 6. However, the Nyquist plots here reported (Figures 7a,b) lack the low-frequency, diffusion-related line, since it was subtracted prior the DRT analysis, satisfying the boundary condition of convergence of the impedance toward the real axis when ω tends to 0, which is not guaranteed with the divergent low-frequency Warburg diffusion.[78,82] The spectra have been fitted by a resistor $R_{el}$, which represents the resistance of the electrolyte and two parallels (RQ) in series, which model the resistance of the passivation layer and the charge transfer resistance, respectively. The calculated DRT

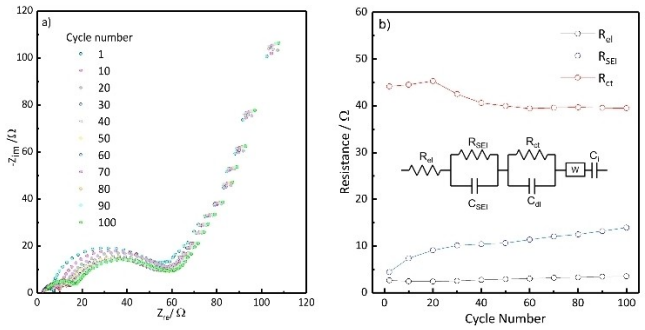


**Figure 6.** (a) Nyquist plot of CCDHC-based SIB electrode prepared with CC–CMC binder, acquired every 10th cycle, E = 0.5 V, 10 mHz < *f* < 100 kHz; (b) Values of $R_{el}$, $R_{SEI}$ and $R_{ct}$ upon cycling, as obtained by EIS data analysis; Equivalent circuit used to simulate the data.

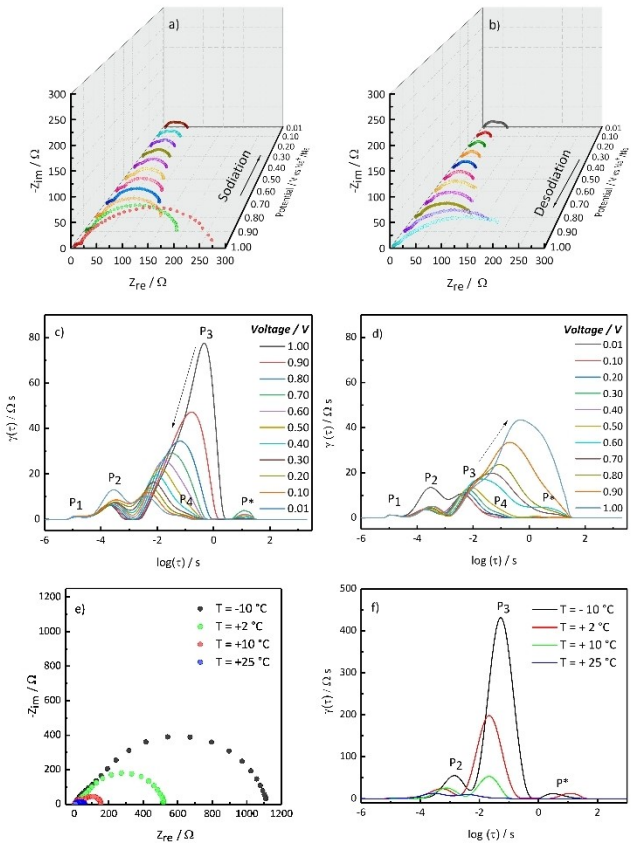


**Figure 7.** Nyquist plot of CCDHC-based SIB electrode prepared with CC–CMC binder, acquired during (a) sodiation and (b) desodiation every 100 mV, 50 mHz < *f* < 100 kHz. Calculated DRT functions during (c) sodiation and (d) desodiation. (e) Nyquist plot acquired at E = 0.01 V at different temperatures, 50 mHz < *f* < 100 kHz; (f) Calculated DRT function at different temperatures.

functions (Figures 7c,d) show three main peaks, and an additional peak marked as P*, which is the residual artifact retained after the removal of the low-frequency line. The peak $P_1$, with a time constant of approximatively $\tau = 1.25 \times 10^{-5}$ s (i.e. high-frequencies) can be attributed to the contact impedance as already reported for graphite in other study.[83] The peak $P_2$, with a time constant of approximatively $\tau = 2.51 \times 10^{-4}$ s, which is consistent with the resistance of the passivation layer ($R_{SEI}$), increases during sodiation and decreases during desodiation as well, consistently with the behavior of the high-frequency semicircle in the Nyquist plots. This behavior suggests that SEI is not completely formed and stabilized after 5 cycles. At 1 V, the most intense peak is $P_3$ with a low time constant of $\tau =$ 0.49 s, corresponding to the medium-frequency semicircle in the Nyquist plot, which can be related to the resistance of charge transfer processes, which is maximum at high potential since no electrochemical reactions occur. Lowering the potential and approaching the sloping region, $P_3$ peak decreases in height and area, and shifts to faster time constant (during sodiation it passes from 0.49 s at 1 V to $1.23 \times 10^{-2}$ s at 0.5 V). Simultaneously, the second semi-circle decreases its diameter in the corresponding Nyquist plots. This means that the resistance associated with the charge transfer $R_{ct}$ progressively decreases upon sodiation and vice versa. Thus, approaching the low voltage plateau, the $P_3$ peaks continue to shift toward lower time constant, reaching a value of approximatively $\tau = 4.05 \times 10^{-3}$ s, and eventually splitting into two contributions, with a new peak $P_4$ appearing below 0.3 V with a higher time constant of $\tau = 5.55 \times 10^{-2}$ s. It is assumed that both peaks are related to the charge transfer process of Hard Carbon. Similar results have been reported for Li–graphite half-cells.[84] Consistently with the cyclic voltammetries, since $P_4$ only appears at low potential upon sodiation, and it is also present upon desodiation at the same potential, it is likely that $P_4$ is related to the intercalation of $Na^+$ ions into the carbon host, while $P_3$ can be assigned to the capacitive adsorption of $Na^+$ ions onto active sites. This is furtherly supported by the fact that the intercalation is expected to be kinetically sluggish compared to the pseudocapacitive adsorption process, hence occurring at higher time constants. In order to better investigate the DRT peaks at the low-voltage plateau, EIS was applied at different temperatures (T = −10, +2, +10, +25 °C) at $E_{we} = 0.01$ V. The corresponding Nyquist plots and the calculated DRT functions are reported in Figure 7e,f. The overall impedance increases, and the DRT peaks increase and shift to the right, when the temperature decreases. The peak $P_2$ shows a moderate temperature dependance, confirming that it describes the SEI polarization. On the other hand, $P_3$ is strongly affected by the temperature, with its intensity rapidly growing as the temperature is lowered. This behavior is typical of an activated charge-transfer process. The peak $P_4$, which is visible below 0.3 V for DRT collected at 25 °C (Figure 7c–d), is not detectable in the graphs of the lower-temperature DRTs because it is probably overlapped by the large-polarization $P_3$ feature.

## Conclusion

High performances HC has been successfully synthesized from biowaste corncobs through a simple one-step carbonization process at 950 °C in inert atmosphere. In parallel, an aqueous binder has been successfully produced from corncob extracted cellulose, by NaOH:$ClCH_2COOH$ etherification, thus obtaining a Na–CMC sample with an estimated degree of substitution of 0.59. By studying the structural and morphological behaviors of the active material, CCHC showed a suitable interlayer spacing and a good surface area for partial bulk insertion and interfacial adsorption of Na. When they are combined in an anode for SIBs, CCDHC active material with CC–CMC binder exhibits good electrochemical performances delivering a specific capacity of 264 mAh $g^{-1}$ at 1 C with a promising capacity retention and good rate capability. Moreover, the electrode shows a high reaction kinetics, while interfacial stability arises from the strong interactions between hard carbon and Na–CMC. According to the experimental observations, the sodium storage arises from the capacitive-controlled adsorption on surface active sites in the sloping region (E > 0.1 V), while the diffusion-controlled intercalation is the predominant process approaching the low-voltage plateau (E < 0.1 V). The reported results represent a relevant contribution both to the in-depth understanding and optimization of the sodium storage mechanisms at carbonaceous hosts, and to the development of high-performing, sustainable anodes for SIBs.

## Experimental Section

### Synthesis of Corncobs-derived Hard Carbon

The corncobs utilized in the experiment were collected from the market food of Marche region (Italy). The corncobs were smashed and dried at 80 °C for 1 day in an oven. Therefore, the dried corncobs were carbonized in a horizontal cylindrical furnace at 950 °C for 2 h under argon flow after a heating ramp of 10 °C/min. The sample was cooled down inside the furnace, under argon flow as well. Finally, the resultant material was ground in an automatic ball mill for 4 h at 300 rpm in a steel jar (ball to powder ratio 1:50 in weight). The fabricated corncobs-derived hard carbon was denoted as CCDHC.

### Isolation of cellulose and synthesis of Corncobs-derived CMC

The raw materials were first ground and dried to remove the excess of water, then three subsequent treatments were preliminary conducted, each followed by a washing step with deionized water until neutral pH. The first treatment was with an aqueous solution of NaOH (3% w/w) at 100 °C for 4 h under vigorous agitation. The second one was a bleaching with an aqueous solution of NaClO (0.1% w/w) at 85 °C for 5 h, using NaOH as buffer (pH ≈12).[85] The third one consisted in a mild acid hydrolysis with 3 M HCl for 1 h at room temperature. Next, for the etherification reaction, the cellulose (dried product) was preliminary immersed in an aqueous solution of NaOH (15% w/w) and stirred for 1 h at room temperature. At the same time, the mixture of chloroacetic acid and ethanol (96% v/v) was added to the batch and stirred for 2 h at 70 °C. The alkali excess was neutralized with some drops of 3 M HCl. The Na–carboxymethyl cellulose was obtained by filtration, fol-

lowed by washing with ethanol and drying. The NaOH:$ClCH_2COOH$ molar ratio was 1.6. The synthesized corncobs-derived CMC was labelled as CC–CMC.

### Material Characterization

Infra-Red spectra of the extracted cellulose, CC–CMC, and standard CMC (ST–CMC) (Sigma Aldrich) powders were recorded by means of a Perkin-Elmer Spectrum Two FTIR spectrometer within the wave number range of 400 to 4000 $cm^{-1}$. Thermogravimetric analysis (TGA) of CCD–CMC was carried out using a Perkin-Elmer STA 6000 Thermal Analyzer. The nitrogen flow rate at the powder was set to 50 mL $min^{-1}$ and an alumina crucible was used to hold the sample. After equilibration, the powder was heated up to 900 °C at a rate of 10 °C $min^{-1}$. The thermogram of synthesized CCD–CMC was compared with that of a commercial analogue (Sigma-Aldrich). $^1$H-Nuclear Magnetic Resonance spectroscopy (NMR) was used to estimate the degree of substitution (DS) of CMC, according to the method proposed by Klosiewict.[86] The method involves the measurement of the ratio of two spectral integrals, A/B, where A is one half of the integral of the carboxymethyl signals in the region between 4.0–4.5 ppm, and B is the integral representing an area of one proton in an anhydroglucose unit. The values of B are obtained using one-sixth of the total integral of the major C–H signals between 3–4 ppm. Before the analysis, the CC–CMC sample was dissolved in deuterium oxide at a concentration of 15 mg/ml heating to 70 °C for 2 h. The spectra were recorded using a Varian Mercury 400 spectrometer operating at 400 MHz. The chemical shifts were quoted in ppm and calibrated from the residual protons signal of deuterated solvent as internal standard. The goodness of the estimation method was assessed applying it to a reference Na–CMC with a DS of 0.90 declared by the manufacturer.

Scanning Electron Microscopy (SEM) and Energy Dispersive X ray analysis (EDX) of the CCDHC sample were acquired using a FESEM Cambridge Stereo scan 360 electron microscope equipped with QUANTAX EDX detector (at an accelerating voltage of 15 kV). The structure of the CCDHC powder was characterized by X-ray diffraction (XRD) (Bragg-Brentano geometry, Cu–Kα, $\lambda = 1.54059$ Å) and Raman spectroscopy (Horiba IHR 320, wavelength 532 nm). The interplanar spacing ($d_{002}$) was calculated according to the Bragg's Law Eq. (8):

$$d_{002} = \lambda / 2\sin(\theta_{002}) \quad (8)$$

with $\lambda = 0.154$ nm.

The crystallite size along c-axis (staked plane height) $L_c$ was estimated according to the Scherrer's Equation Eq. (9):

$$L_c = K\,\lambda / \beta_{002}\cos(\theta_{002}) \quad (9)$$

where K is a shape factor which corresponds to 0.9 and β is the full width at half maximum of (002) peak.[87] Moreover, the average width of graphene domain $L_a$ was also estimated using Raman technique according to the Eq. (10):

$$L_\alpha = (2.4\,E^{-10})\,\lambda^4\,(I_G/I_D) \quad (10)$$

where λ is the wavelength of laser source (532 nm) and $I_G/I_D$ is the intensity ratio between the D band over the G band.

Pore characteristics of CCDHC were evaluated by $N_2$ adsorption/desorption measurement at 77 K and $CO_2$ adsorption measurement at 273 K using a Micromeritics ASAP 2020 instrument. Prior to both the adsorption/desorption measurements, the CCDHC sample had been outgassed for 12 h at 150 °C. The specific surface area was calculated by the BET model over the classical range $p/p^0 = 0.05$–0.3.

### Electrode Preparation and Cell Assembling

Negative electrodes were made with CCDHC as the active material, Super-P carbon (Imerys) as the conductive agent, and CC–CMC as the binder. CCDHC:Super-P:CCD–CMC (85:10:5 w/w) slurries were prepared in high purity deionized water, coated onto Cu foil using the doctor blade technique (thickness of wet coating = 100 μm), and left to dry at r.t.. After calendaring, circular electrodes (9 mm diameter) were cut and further dried at 120 °C under vacuum for 12 h. The loading of active material was around 1.5 mg $cm^{-2}$ for all the electrodes. For the half-cell, three-electrode Swagelok-type cells were assembled in an argon-filled glove box (Jacomex GP-campus, oxygen and moisture content less than 0.8 ppm) using CCDHC as working electrode and metallic sodium (Sigma-Aldrich) as reference and counter electrodes. A 1 M solution of $NaClO_4$ (Sigma-Aldrich) in ethylene carbonate (EC)/polycarbonate (PC) (1:1 in volume) (Sigma-Aldrich) was selected as the electrolyte (400 μl) and 12 mm glass fiber disks (Whatman GF/A) as separator. After the assembly, the cells were removed from the glove box for the electrochemical characterization.

### Electrochemical Characterization

All electrochemical tests were carried out using a VMP-2Z multichannel electrochemical workstation by Bio-Logic Science Instruments (France). Cyclic voltammetry of the sample was carried out at different scanning rates ranging from 0.10 mV $s^{-1}$ to 1.00 mV $s^{-1}$ in the voltage range 0.01 to 2 V. Galvanostatic charge/discharge and rate capability tests of the electrodes were collected with the voltage ranging between 0.01 and 2 V. For all the experiments, 1 C rate was assumed as 300 mA/g with respect to active material mass. In addition, C-rate capability of the CCDHC electrode was evaluated in the C/5 to 5 C range (5 cycles at every rate). In order to evaluate the interfacial behavior of electrodes, electrochemical impedance spectroscopy (EIS) was carried out at the first cycle and then at each tenth cycle at E = 0.5 V, with an AC amplitude of 5 mV, in a frequency range 100 kHz $> f >$ 10 mHz. Additionally, to deeply understand the interfacial and the sodium storage behaviours of CCDHC, staircase potentio impedance spectroscopy (SPEIS) was carried out during sodiation and desodiation. The impedance measurements were carried out at 5$^{th}$ cyle, setting potential step of 100 mV from 1.00 to 0.01 V, applying the same pulse of 5 mV amplitude as for EIS each tenth cycle, in the frequency range from 100 kHz to 50 mHz. The SPEIS data analysis was performed by Distribution of Relaxation Times (DRT) and Equivalent Circuit Model (ECM) methods. All potentials are given vs. $Na^+/Na$ redox couple ($E° = -2.7$ vs. SHE).

## Acknowledgements

*The authors gratefully acknowledge funding support for this work from: (i) University of Camerino within the FAR (Fondi di Ateneo per la Ricerca) funding scheme, project "yieLding added valuE to Apennine Forest resources (LEAF)"; (ii) ENEA (Agenzia Nazionale per le Nuove Tecnologie, l'Energia e lo Sviluppo Sostenibile) and MiSE (Ministero per lo Sviluppo Economico) within the project: "Sistemi di Accumulo di Energia per il Sistema Elettrico" in the framework of PTR Program.*

## Conflict of Interest

The authors declare no conflict of interest.

## Data Availability Statement

The data that support the findings of this study are available from the corresponding author upon reasonable request.

**Keywords:** Anode · Binder · DRT · EIS · Hard Carbon

[1] M. D. Slater, D. Kim, E. Lee, C. S. Johnson, *Adv. Funct. Mater.* **2013**, *23*, 947–958.
[2] T. Liu, Y. Zhang, Z. Jiang, X. Zeng, J. Ji, Z. Li, X. Gao, M. Sun, Z. Lin, M. Ling, J. Zheng, C. Liang, *Energy Environ. Sci.* **2019**, *12*, 1512–1533.
[3] H. Pan, Y. S. Hu, L. Chen, *Energy Environ. Sci.* **2013**, *6*, 2338–2360.
[4] J. Y. Hwang, S. T. Myung, Y. K. Sun, *Chem. Soc. Rev.* **2017**, *46*, 3529–3614.
[5] K. Chayambuka, G. Mulder, D. L. Danilov, P. H. L. Notten, *Adv. Energy Mater.* **2018**, *8*, 1–49.
[6] J. Janek, W. G. Zeier, *Nat. Energy* **2016**, *1*, 1–4.
[7] J. M. Tarascon, *Nat. Chem.* **2010**, *2*, 510.
[8] C. Grosjean, P. Herrera Miranda, M. Perrin, P. Poggi, *Renewable Sustainable Energy Rev.* **2012**, *16*, 1735–1744.
[9] Z. P. Cano, D. Banham, S. Ye, A. Hintennach, J. Lu, M. Fowler, Z. Chen, *Nat. Energy* **2018**, *3*, 279–289.
[10] C. Vaalma, D. Buchholz, M. Weil, S. Passerini, *Nat. Rev. Mater.* **2018**, *3*, 18013.
[11] P. Gupta, S. Pushpakanth, M. A. Haider, S. Basu, *ACS Omega* **2022**, *7*, 5605–5614.
[12] S. Y. Hong, Y. Kim, Y. Park, A. Choi, N. S. Choi, K. T. Lee, *Energy Environ. Sci.* **2013**, *6*, 2067–2081.
[13] L. Zhao, T. Zhang, W. Li, T. Li, L. Zhang, X. Zhang, Z. Wang, *Engineering* **2022**, In Press, Journal Pre-proof.
[14] K. M. Abraham, *ACS Energy Lett.* **2020**, *5*, 3544–3547.
[15] K. Nobuhara, H. Nakayama, M. Nose, S. Nakanishi, H. Iba, *J. Power Sources* **2013**, *243*, 585–587.
[16] H. Kim, J. Hong, Y. U. Park, J. Kim, I. Hwang, K. Kang, *Adv. Funct. Mater.* **2015**, *25*, 534–541.
[17] P. Bai, Y. He, P. Xiong, X. Zhao, K. Xu, Y. Xu, *Energy Storage Mater.* **2018**, *13*, 274–282.
[18] Y. Li, Y. S. Hu, M. M. Titirici, L. Chen, X. Huang, *Adv. Energy Mater.* **2016**, *6*, 1600659.
[19] X. Dou, I. Hasa, D. Saurel, C. Vaalma, L. Wu, D. Buchholz, D. Bresser, S. Komaba, S. Passerini, *Mater. Today* **2019**, *23*, 87–104.
[20] P. Bai, X. Han, Y. He, P. Xiong, Y. Zhao, J. Sun, Y. Xu, *Energy Storage Mater.* **2020**, *25*, 324–333.
[21] F. Shen, W. Luo, J. Dai, Y. Yao, M. Zhu, E. Hitz, Y. Tang, Y. Chen, V. L. Sprenkle, X. Li, L. Hu, *Adv. Energy Mater.* **2016**, *6*, 1–7.
[22] J. Wang, H. Yin, Y. Xu, Z. Chen, J. Gao, Z. Wang, S. Zuo, *Ind. Crops Prod.* **2023**, *192*, 116079.
[23] W. Lv, F. Wen, J. Xiang, J. Zhao, L. Li, L. Wang, Z. Liu, Y. Tian, *Electrochim. Acta* **2015**, *176*, 533–541.
[24] H. Moon, A. Innocenti, H. Liu, H. Zhang, M. Weil, M. Zarrabeitia, S. Passerini, *ChemSusChem* **2023**, *16*, e202202263.
[25] T. Zhang, J. Mao, X. Liu, M. Xuan, K. Bi, X. L. Zhang, J. Hu, J. Fan, S. Chen, G. Shao, *RSC Adv.* **2017**, *7*, 41504–41511.
[26] P. C. Rath, J. Patra, H. T. Huang, D. Bresser, T. Y. Wu, J. K. Chang, *ChemSusChem* **2019**, *12*, 2302–2309.
[27] K. L. Hong, L. Qie, R. Zeng, Z. Q. Yi, W. Zhang, D. Wang, W. Yin, C. Wu, Q. J. Fan, W. X. Zhang, Y. H. Huang, *J. Mater. Chem. A* **2014**, *2*, 12733–12738.
[28] E. M. Lotfabad, J. Ding, K. Cui, A. Kohandehghan, W. P. Kalisvaart, M. Hazelton, D. Mitlin, *ACS Nano* **2014**, *8*, 7115–7129.
[29] H. Darjazi, L. Bottoni, H. R. Moazami, S. J. Rezvani, L. Balducci, L. Sbrascini, *Mater. Today Sustain.* **2023**, *21*, 100313.
[30] N. Zhang, Q. Liu, W. Chen, M. Wan, X. Li, L. Wang, L. Xue, W. Zhang, *J. Power Sources* **2018**, *378*, 331–337.
[31] J. A. Elegbede, V. A. Ajayi, A. Lateef, *Environ. Technol. Innov.* **2021**, *24*, 102073.
[32] P. Bai, Y. He, X. Zou, X. Zhao, P. Xiong, Y. Xu, *Adv. Energy Mater.* **2018**, *8*, 1–9.
[33] S. Alvin, H. S. Cahyadi, J. Hwang, W. Chang, S. K. Kwak, J. Kim, *Adv. Energy Mater.* **2020**, *10*, 1–16.
[34] D. A. Stevens, J. R. Dahn, *J. Electrochem. Soc.* **2000**, *147*, 4428.
[35] C. Bommier, T. W. Surta, M. Dolgos, X. Ji, *Nano Lett.* **2015**, *15*, 5888–5892.
[36] X. Liu, T. Wang, T. Ji, H. Wang, H. Liu, J. Li, D. Chao, *J. Mater. Chem. A* **2022**, *10*, 8031–8046.
[37] B. Zhang, C. M. Ghimbeu, C. Laberty, C. Vix-Guterl, J. M. Tarascon, *Adv. Energy Mater.* **2016**, *6*, 1–9.
[38] X. Chen, C. Liu, Y. Fang, X. Ai, F. Zhong, H. Yang, Y. Cao, *Carbon Energy* **2022**, *4*, 1–18.
[39] D. Bresser, D. Buchholz, A. Moretti, A. Varzi, S. Passerini, *Energy Environ. Sci.* **2018**, *11*, 3096–3127.
[40] P. S. Salini, S. V. Gopinadh, A. Kalpakasseri, B. John, M. Thelakkattu Devassy, *ACS Sustainable Chem. Eng.* **2020**, *8*, 4003–4025.
[41] M. Mancini, F. Nobili, R. Tossici, M. Wohlfahrt-Mehrens, R. Marassi, *J. Power Sources* **2011**, *196*, 9665–9671.
[42] J. S. Kim, Y. Y. Lee, T. H. Kim, *Bioresour. Technol.* **2016**, *199*, 42–48.
[43] L. Brinchi, F. Cotana, E. Fortunati, J. M. Kenny, *Carbohydr. Polym.* **2013**, *94*, 154–169.
[44] T. Shui, S. Feng, G. Chen, A. Li, Z. Yuan, H. Shui, T. Kuboki, C. Xu, *Biomass Bioenergy* **2017**, *105*, 51–58.
[45] G. Joshi, S. Naithani, V. K. Varshney, S. S. Bisht, V. Rana, P. K. Gupta, *Waste Manage.* **2015**, *38*, 33–40.
[46] M. S. Yeasmin, M. I. H. Mondal, *Int. J. Biol. Macromol.* **2015**, *80*, 725–731.
[47] N. Haleem, M. Arshad, M. Shahid, M. A. Tahir, *Carbohydr. Polym.* **2014**, *113*, 249–255.
[48] M. Akram, I. Taha, M. M. Ghobashy, *Cellulose* **2016**, *23*, 1713–1724.
[49] C. M. Obele, M. E. Ibenta, J. L. Chukwuneke, S. C. Nwanonenyi, *Cellulose* **2021**, *28*, 2615–2633.
[50] Y. Li, Y. S. Hu, H. Li, L. Chen, X. Huang, *J. Mater. Chem. A* **2015**, *4*, 96–104.
[51] X. Zhu, X. Jiang, X. Liu, L. Xiao, Y. Cao, *Green Energy & Environ.* **2017**, *2*, 310–315.
[52] R. F. Susanti, S. Alvin, J. Kim, *J. Ind. Eng. Chem.* **2020**, *91*, 317–329.
[53] S. Puravankara, Nagmani, *ACS Appl. Energ. Mater.* **2020**, *3*, 10045–10052.
[54] K. Wang, Y. Jin, S. Sun, Y. Huang, J. Peng, J. Luo, Q. Zhang, Y. Qiu, C. Fang, J. Han, *ACS Omega* **2017**, *2*, 1687–1695.
[55] A. Beda, P. L. Taberna, P. Simon, C. Matei Ghimbeu, *Carbon* **2018**, *139*, 248–257.
[56] H. Darjazi, A. Staffolani, L. Sbrascini, L. Bottoni, R. Tossici, F. Nobili, *Energies* **2020**, *13*, 6216.
[57] S. Ghosh, R. Santhosh, S. Jeniffer, V. Raghavan, G. Jacob, K. Nanaji, P. Kollu, S. K. Jeong, A. N. Grace, *Sci. Rep.* **2019**, *9*, 1–15.
[58] C. Chen, Y. Huang, Y. Zhu, Z. Zhang, Z. Guang, Z. Meng, P. Liu, *ACS Sustainable Chem. Eng.* **2020**, *8*, 1497–1506.
[59] C. Matei Ghimbeu, J. Górka, V. Simone, L. Simonin, S. Martinet, C. Vix-Guterl, *Nano Energy* **2018**, *44*, 327–335.
[60] V. Velez, G. Ramos-Sánchez, B. Lopez, L. Lartundo-Rojas, I. González, L. Sierra, *Carbon* **2019**, *147*, 214–226.
[61] M. Liu, J. Zhang, S. Guo, B. Wang, Y. Shen, X. Ai, H. Yang, J. Qian, *ACS Appl. Mater. Interfaces* **2020**, *12*, 17620–17627.
[62] M. Zhang, Y. Li, F. Wu, Y. Bai, C. Wu, *Nano Energy* **2021**, *82*, 105738.
[63] N. Sun, H. Liu, B. Xu, *J. Mater. Chem. A* **2015**, *3*, 20560–20566.
[64] X. Li, X. Zeng, T. Ren, J. Zhao, Z. Zhu, S. Sun, Y. Zhang, *J. Alloys Compd.* **2019**, *787*, 229–238.
[65] M. Zarrabeitia, M. Á. Muñoz-Márquez, F. Nobili, T. Rojo, M. Casas-Cabanas, *Batteries* **2017**, *3*, 1–13.
[66] J. Conder, C. Villevieille, *Chem. Commun.* **2019**, *55*, 1275–1278.
[67] J. Ding, H. Wang, Z. Li, A. Kohandehghan, K. Cui, Z. Xu, B. Zahiri, X. Tan, E. M. Lotfabad, B. C. Olsen, D. Mitlin, *ACS Nano* **2013**, *7*, 11004–11015.
[68] Q. Jin, K. Wang, P. Feng, Z. Zhang, S. Cheng, K. Jiang, *Energy Storage Mater.* **2020**, *27*, 43–50.
[69] V. Augustyn, J. Come, M. A. Lowe, J. W. Kim, P. L. Taberna, S. H. Tolbert, H. D. Abruña, P. Simon, B. Dunn, *Nat. Mater.* **2013**, *12*, 518–522.
[70] S. Qiu, L. Xiao, M. L. Sushko, K. S. Han, Y. Shao, M. Yan, X. Liang, L. Mai, J. Feng, Y. Cao, X. Ai, H. Yang, J. Liu, *Adv. Energy Mater.* **2017**, *7*, 1–11.
[71] J. Yang, Z. Ju, Y. Jiang, Z. Xing, B. Xi, J. Feng, S. Xiong, *Adv. Mater.* **2018**, *30*, 1700104.
[72] Y. Liu, H. Dai, L. Wu, W. Zhou, L. He, W. Wang, W. Yan, Q. Huang, L. Fu, Y. Wu, *Adv. Energy Mater.* **2019**, *9*, 1–9.
[73] N. Sun, Z. Guan, Y. Liu, Y. Cao, Q. Zhu, H. Liu, Z. Wang, P. Zhang, B. Xu, *Adv. Energy Mater.* **2019**, *9*, 1–14.

[74] T. Brezesinski, J. Wang, S. H. Tolbert, B. Dunn, *Nat. Mater.* **2010**, *9*, 146–151.
[75] A. Beda, F. Rabuel, M. Morcrette, S. Knopf, P. L. Taberna, P. Simon, C. Matei Ghimbeu, *J. Mater. Chem. A* **2021**, *9*, 1743–1758.
[76] J. Wang, L. Yan, Q. Ren, L. Fan, F. Zhang, Z. Shi, *Electrochim. Acta* **2018**, *291*, 188–196.
[77] F. Nobili, S. Dsoke, M. Mancini, R. Tossici, R. Marassi, *J. Power Sources* **2008**, *180*, 845–851.
[78] L. Sbrascini, A. Staffolani, L. Bottoni, H. Darjazi, L. Minnetti, M. Minicucci, F. Nobili, *ACS Appl. Mater. Interfaces* **2022**, *14*, 33257–33273.
[79] J.-H. Lee, U. Paik, V. A. Hackley, Y.-M. Choi, *J. Electrochem. Soc.* **2005**, *152*, A1763.
[80] R. Mogensen, D. Brandell, R. Younesi, *ACS Energy Lett.* **2016**, *1*, 1173–1178.
[81] L. A. Ma, A. J. Naylor, L. Nyholm, R. Younesi, *Angew. Chem. Int. Ed.* **2021**, *60*, 4855–4863; *Angew. Chem.* **2021**, *133*, 4905–4913.
[82] K. Pan, F. Zou, M. Canova, Y. Zhu, J. H. Kim, *J. Power Sources* **2020**, *479*, 229083.
[83] P. Shafiei Sabet, G. Stahl, D. U. Sauer, *J. Power Sources* **2020**, *472*, 228189.
[84] X. Chen, L. Li, M. Liu, T. Huang, A. Yu, *J. Power Sources* **2021**, *496*, 229867.
[85] C. Liu, B. Li, H. Du, D. Lv, Y. Zhang, G. Yu, X. Mu, H. Peng, *Carbohydr. Polym.* **2016**, *151*, 716–724.
[86] D. W. Klosiewict, *Anal. Chem.* **1980**, *52*, 913–916.
[87] C. Nita, B. Zhang, J. Dentzer, C. Matei Ghimbeu, *J. Energy Chem.* **2021**, *58*, 207–218.

Manuscript received: November 29, 2022
Revised manuscript received: February 8, 2023
Version of record online: ■■, ■■

# RESEARCH ARTICLE

**Hard carbon for sodium-ion batteries**: Corncobs are used for the preparation of bio-based electrode with hard carbon as active material and carboxymethyl cellulose as binder. The electrodes deliver a high discharge capacity and good rate capability. Additionally, the sodium storage behavior of Hard Carbons was investigated.

*L. Bottoni*, Dr. H. Darjazi, L. Sbrascini, Dr. A. Staffolani, Prof. S. Gabrielli, Dr. G. Pastore, Dr. A. Tombesi, Prof. F. Nobili*

1 – 12

**Electrochemical Characterization of Charge Storage at Anodes for Sodium-Ion Batteries Based on Corncob Waste-Derived Hard Carbon and Binder**

Special Collection